Preclinical Characterization of $^{86/90}$Y-NM600 in a Variety of Murine and Human Cancer Tumor Models

Joseph J. Grudzinski[1], Reinier Hernandez[2], Ian Marsh[1], Ravi B. Patel[3], Eduardo Aluicio-Sarduy[1], Jon Engle[1,2], Zachary Morris[3], Bryan Bednarz[1–3], and Jamey Weichert[1,2,4]

[1]Department of Medical Physics, University of Wisconsin–Madison, Madison, Wisconsin; [2]Department of Radiology, University of Wisconsin, Madison, Wisconsin; [3]Department of Human Oncology, University of Wisconsin–Madison, Madison, Wisconsin; and [4]University of Wisconsin Carbone Cancer Center, Madison, Wisconsin

We characterize the in vivo biodistribution and tumor selectivity of ^{86}Y-NM600, a theranostic alkylphosphocholine radiometal chelate with broad tumor selectivity, in a variety of preclinical cancer models. **Methods:** Mice bearing flank tumors (representative of lung, pancreatic, prostate, liver, skin, and lymphoid cancers) were injected intravenously with 9.25 MBq of ^{86}Y-NM600 and imaged longitudinally over 4–5 d using small-animal PET/CT. Percentage injected activity per gram (%IA/g) for each volume of interest was measured at each time point for the organs of interest. Mice were euthanized after the final time point, and the tumor and organs of interest were counted with an automatic γ-counter. Absorbed doses delivered by ^{90}Y-NM600 per injected activity (Gy/MBq) were estimated. Mice bearing B78 flank tumors were injected with a prescription of ^{90}Y-NM600 that delivered 2.5 Gy of absorbed tumor dose and was compared with an equivalent absorbed dose delivered via external-beam radiotherapy using tumor volume as a measure of response. Histology and complete blood counts were analyzed in naïve C57BL/6 mice that were injected with 9.25 MBq of ^{90}Y-NM600 at 5, 10, and 28 d after injection. **Results:** PET imaging showed consistent tumor accumulation and retention across all tumor models investigated, with little off-target retention of NM600 except in the liver, as is characteristic of hepatobiliary metabolism. The tumor uptake was highest in the pancreatic and lymphoid cancer models, reaching peak concentrations of 9.34 ± 2.66 %IA/g (n = 3) and 9.10 ± 0.13 %IA/g (n = 3), respectively, at approximately 40–48 h after injection. These corresponded to tumor dose estimates of 2.72 ± 0.33 Gy/MBq and 2.67 ± 0.32 Gy/MBq, respectively. In the toxicity study, there were no visible signs of acute toxicity by histology, and perturbation of hematologic parameters was transient when observed, returning to pretherapy levels after 28 d. **Conclusion:** NM600 is a theranostic agent with a unique ability to selectively target a variety of cancer types, presenting a unique opportunity for PET image–guided targeted radionuclide therapy and combination with immunotherapies.

Key Words: NM600; targeted radionuclide therapy; immunomodulation; theranostics

J Nucl Med 2019; 60:1622–1628
DOI: 10.2967/jnumed.118.224808

The selective uptake and prolonged retention of antitumor alkylphosphocholines have been attributed to the selective insertion of these compounds into areas of cell membranes that contain large accumulations of sphingolipids and cholesterol known as lipid rafts (*1–5*). The alkylphosphocholine-DOTA metal chelate, NM600 (Fig. 1), can be radiolabeled with a variety of radiometals for both targeted radionuclide therapy (TRT) (e.g., ^{90}Y, ^{177}Lu, and ^{225}Ac) and PET imaging (e.g., ^{86}Y, ^{64}Cu, and ^{89}Zr). ^{90}Y, which has unique properties that may be conducive to immunomodulation, is a pure β-emitter with a 3.9-mm mean pathlength enabling the delivery of radiotherapy throughout the tumor microenvironment, including islands of stromal cells, while sparing bone marrow, spleen, and draining lymphatics. In addition, its physical half-life (2.67 d) pairs well with the pharmacokinetic profile of alkylphosphocholine chelates, is not too short to preclude integration into clinical workflows, and is not so long as to interfere with timely generation of an effective antitumor immune response after delivering immununomodulatory low-dose TRT to the tumor microenvironment. Furthermore, ^{90}Y has an isosteric PET theranostic pair. ^{86}Y-NM600 PET can be used to estimate ^{90}Y in vivo 3-dimensional biodistribution and dosimetry.

The primary aim of this work was to evaluate the in vivo biodistribution of NM600 in a variety of preclinical cancer models and estimate its effectiveness to precisely and safely deliver targeted immunomodulatory TRT using ^{90}Y-NM600. The secondary aim of this work was to test whether ^{86}Y-NM600 could be used to estimate ^{90}Y-NM600 dosimetry estimations for treatment planning of a TRT preclinical trial.

MATERIALS AND METHODS

Radiosynthesis of $^{86/90}$Y-NM600

The production of ^{86}Y and radiolabeling of NM600 have been described elsewhere (*6*). ^{86}Y was produced in a PETrace biomedical cyclotron via bombardment of enriched ^{86}Sr-$SrCO_3$ (96.4% ± 0.1%) targets with 16-MeV protons. After irradiation, targets were dissolved in 6N HCl, loaded onto an extraction resin functionalized with *N,N,N′,N′*-tetrakis-2-ethylhexyldiglycolamide (branched DGA, Eichrom), and washed with diluted H_3NO_3 (0.01 M), and ^{86}Y was quantitatively eluted from the column in less than 600 μL of 0.1 M HCl. $^{90}YCl_3$, purchased from Perkin Elmer, was used without further purification. Radiolabeling of NM600 with ^{86}Y and ^{90}Y was performed with the same specific activity by buffering 185–370 MBq (5−10 mCi) of $^{86/90}$Y with 0.1 M NaOAc (pH 5.5) and adding 296 nmol/GBq (10 μg/mCi) of NM600. The reaction was incubated for 30 min at 90°C under constant shaking (500 rpm). $^{86/90}$Y-NM600 was

Received Dec. 11, 2018; revision accepted Mar. 26, 2019.
For correspondence or reprints contact: Joseph J. Grudzinski, Wisconsin Institutes for Medical Research, 1111 Highland Ave., Room 1005, Madison, WI 53705.
E-mail: grudzinski@wisc.edu
Published online Apr. 6, 2019.

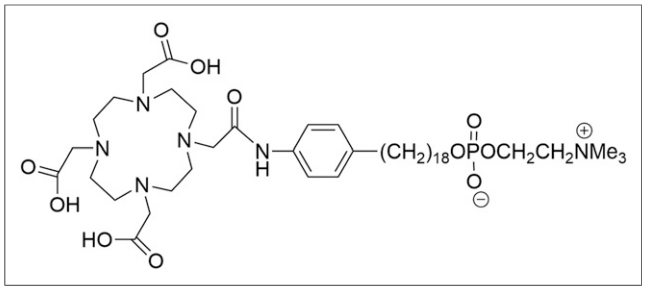

FIGURE 1. Schematic representation of NM600.

purified by a solid-phase extraction cartridge (HLB; Waters) and eluted in 2 mL of 200-proof ethanol. The eluate was then evaporated under a nitrogen stream, and $^{86/90}$Y-NM600 was reconstituted in excipient (saline containing 0.4% v/v polysorbate 20). Radiolabeling yield and radiochemical purity were assessed by instant thin-layer chromatography using silica-impregnated paper as the stationary phase and run using 50 mM ethylenediaminetetraacetic acid. Instant thin-layer chromatography chromatograms were developed using a cyclone phosphor-plate imager and analyzed with Optiquant software (Perkin Elmer).

Imaging and Biodistribution

All animal studies were performed under the approval of the University of Wisconsin Institutional Animal Care and Use Committee. Mice bearing B78 (*7*), EL-4 (ATCC TIB-39), LLC (ATCC CRL-1642), Panc02 (*8*), Myc-Cap (*9*), Hut 102 (*10*), HCT 116 (ATCC CCL-247), or A549 (ATCC CCL-185) xenografts (n = 3/group) were injected intravenously in the lateral tail vein with 9.25 MBq (2.7 nmol) of ^{86}Y-NM600 and longitudinally scanned with an Inveon small-animal PET/CT scanner (Siemens Medical Solutions) 4 separate times over 4 or 5d after injection of the radiotracer. The static PET scans (time window, 3.432 ns; energy window, 350–650 keV), which were terminated after 80 million coincidence events, were followed by CT scans (80 kVp; 1,000 mAs; 220 angles). Before each scan, mice were anesthetized with isoflurane (4% induction; 2% maintenance) and placed prone on the scanner bed. List-mode PET scans were reconstructed using 3-dimensional ordered-subset expectation maximization, and the resulting images were coregistered with the CT images, which were used for attenuation correction, anatomic reference, and estimation of tissue density, which is used for dosimetry calculations. Volume-of-interest (VOI) analysis of the PET images was performed to determine the magnitude and rate of ^{86}Y-NM600 uptake in tumor and nontumor tissues. The biologic half-life of the blood was determined by fitting the time–activity curve to a monoexponential function. Quantitative data were expressed as percentage injected activity per gram of tissue (%IA/g; mean ± SD). The same VOIs were used as target organs in the dosimetry analysis. Using the CT for anatomic reference and density-based thresholding, VOIs were drawn that encompassed the entire mouse volume. A separate contour was made for the brain, lungs, heart (blood pool), liver, kidneys (right and left separately), spinal cord, skeleton, and bladder (urine contents). Cavities of low density within each femur were contoured using thresholding to represent bone marrow of the left and right femurs. After all VOIs were delineated, the remainder of the body was contoured (whole body).

Ex vivo biodistribution was performed after the final imaging time point to corroborate the accuracy of the image-derived quantification and determine additional biodistribution data. After PET/CT, the mice were sacrificed by CO_2 asphyxiation. Tumors, along with several nontumor tissues, were collected, wet-weighed, and counted in an automated γ-counter (Wizard 2; Perking Elmer), and the %ID/g (mean ± SD) was calculated for each tissue. There were regions in some larger tumors that were visibly necrotic. These regions of nonviable tissue correlated with regions that were devoid of signal in the PET images. Therefore, these regions were excluded from γ-counting and were not contoured on the PET/CT images.

Dosimetry Estimation

A Monte Carlo–based dosimetry assessment platform, RAPID (Radionuclide Assessment Platform for Internal Dosimetry), was used to estimate preclinical dose distributions in mouse-specific anatomy (*11,12*). ^{86}Y-NM600 activity concentration was converted to ^{90}Y-NM600 uptake at each time point by correcting for the difference in physical decay rates. CT and the PET images were used in the Monte Carlo simulation to define the geometry and the source distribution, respectively. The processing of the PET/CT volumes in the Monte Carlo framework (Geant4, version 9.6) and generation of 3-dimensional cumulative dose distribution (0.42 × 0.42 × 0.42 mm) are described elsewhere (*13*). The dose rate in each VOI was then integrated over time to calculate cumulative dose using a hybrid of trapezoidal and analytic integration. CT-based contours of the tumor and organs of interest were used to quantify the in vivo concentration of NM600 over time (pharmacokinetics) and describe the spatial distribution of the absorbed dose imparted by ^{90}Y-NM600 (dosimetry).

Toxicity Evaluation

Complete blood count and histologic studies were performed on naïve mice to evaluate ^{90}Y-NM600 toxicity. A group of 10- to 12-wk-old C57BL/6 naïve mice (n = 12) were administered 9.25 MBq (2.7 nmol) of ^{90}Y-NM600 or excipient (control) intravenously. Three mice were sacrificed at days 5, 10, and 28 after injection, and approximately 500 μL of blood were collected for a comprehensive complete blood count analysis using the VetScan VS2 (Abaxis). Additionally, potential organs at risk for radiotoxicity, including the liver, kidney, spleen, small intestine, and bone marrow, were collected, fixed, sectioned, and

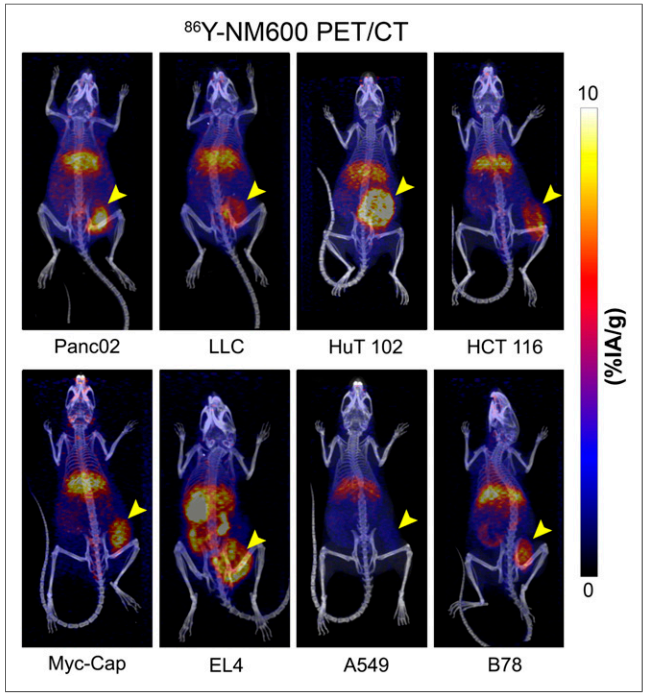

FIGURE 2. Volume rendering of PET overlaid on CT at final time point for each tumor model. Data are decay-corrected, and tumors are on right flank.

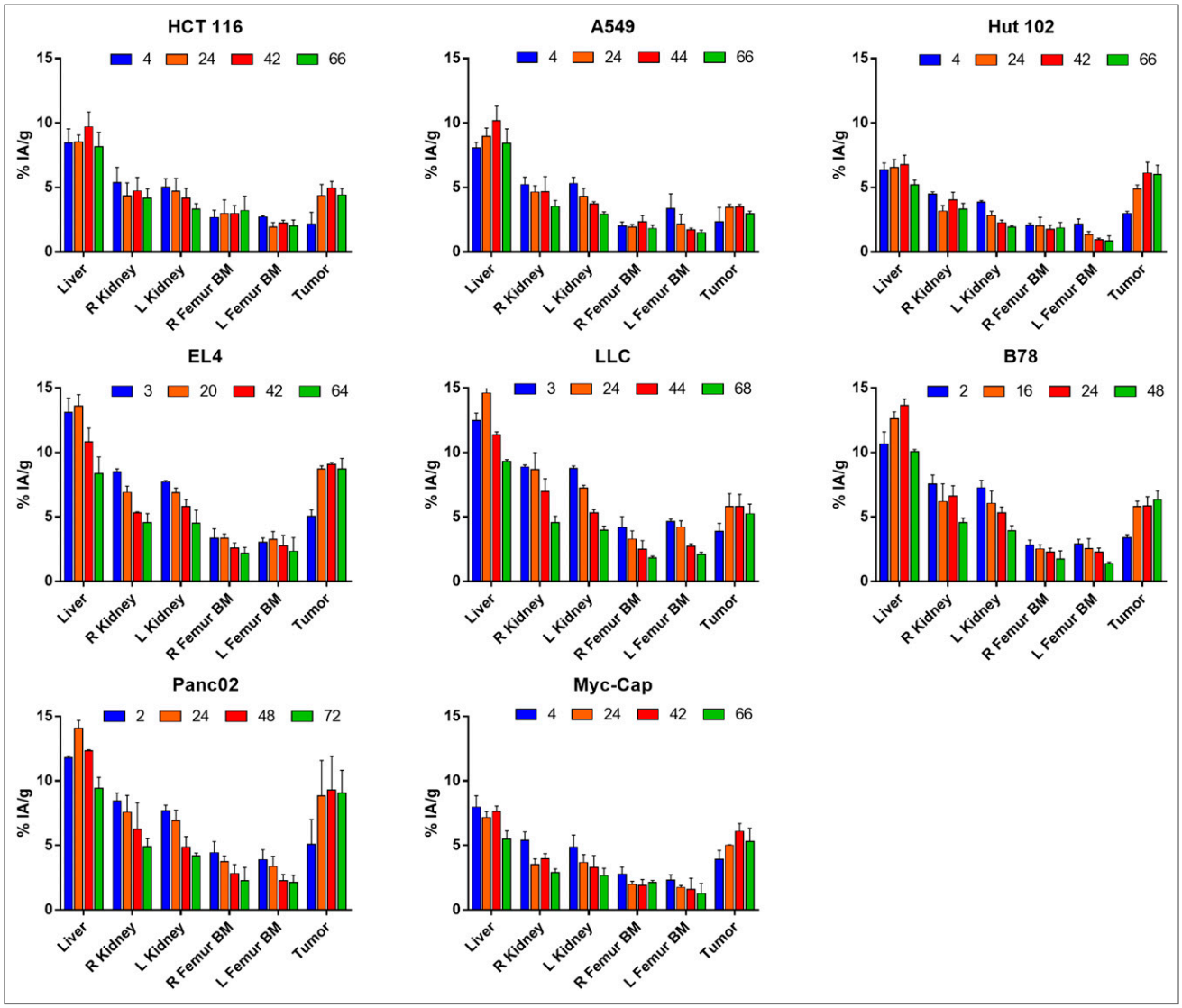

FIGURE 3. In vivo biodistribution. Mean (±SD) %IA/g of each VOI is charted for each tumor model ($n = 3$). In vivo biodistribution measured via PET imaging showed consistent tumor accumulation and retention across all tumor models investigated, with little off-target retention of NM600 except in liver, as is characteristic of hepatobiliary clearance. At early time points in distribution phase, there was elevated uptake of NM600 in highly perfused tissues such as kidneys. In later time points in clearance phase, NM600 washed out of highly perfused tissues.

hematoxylin- and eosin-stained for histopathologic analysis. Blood chemistry and histology were compared with control mice.

Efficacy Evaluation

Using the longitudinal ^{86}Y-NM600 PET imaging of B78 and RAPID, we performed a therapy study to test whether we could, first, cause tumor responses with ^{90}Y-NM600 TRT like those with external-beam radiotherapy (XRT) and, second, validate our dosimetry methodology of using theranostic NM600 and RAPID. To that end, mice bearing flank B78 tumors ($n = 18$) were either irradiated with 2.5 Gy XRT, administered an activity of ^{90}Y-NM600 that was calculated to deliver 2.5 Gy to the tumor, or injected with phosphate-buffered saline. Calipers were used to measure tumor volume (volume = (width^2 × length)/2) biweekly and assess dose response.

Statistical Analysis

To ensure the statistical power of the acquired data, a minimum sample size of 3 for in vivo small-animal PET/CT imaging experiment and 6 for treatment groups was used. Quantitative data were expressed as mean ± SD. Statistical analysis was performed using GraphPad Prism, version 7.00 (GraphPad Software), for Windows (Microsoft). To estimate how time interacts with the groups of the treatment study, a linear mixed model was fit to the data with both a random slope and intercept for our subject indicator. Approximate P values were found using the Satterwhite approximation in R.

RESULTS

Imaging and Biodistribution

In vivo biodistribution measured via PET imaging showed consistent tumor accumulation and retention across all tumor models investigated, with little off-target retention of NM600, except in the liver (Fig. 2; Supplemental Fig. 1; supplemental materials are available at http://jnm.snmjournals.org/). At early time points during the distribution phase, there was elevated

TABLE 1
Average Blood Half-Life and Peak Tumor Uptake for Each Tumor Type

Cell type	Half-life (h)	Peak uptake (%IA/g)
HCT 116	40.5	5.0
A549	39.8	3.5
EL4	26.7	9.1
B78	28.6	6.3
LLC	33.1	5.8
Hut 102	29.7	6.1
Panc02	38.8	9.3
Myc-Cap	27.6	6.1
Average	33.1 (SD, 5.8)	6.4 (SD, 1.9)

uptake of NM600 in highly perfused tissues such as the heart (blood pool), kidneys, and lungs. At later time points during the clearance phase, NM600 washed out of the highly perfused tissues. In contrast, there were low levels of uptake within the bone marrow, fat, and muscle. The organ with the highest levels of retention was the liver, as is consistent with hepatobiliary metabolism and clearance of alkylphosphocholines (Fig. 3). The 2 tumor models with the highest average tumor uptake were Panc02 and EL4, which reached concentrations of 9.34 ± 2.66 %IA/g (n = 3) and 9.10 ± 0.13 %IA/g (n = 3), respectively, at approximately 40–48 h after injection. The tumor type with the lowest peak tumor concentration was A549, with 3.51 ± 0.19 %IA/g (n = 3). The average peak of all tumor types investigated was 6.40 ± 0.82 %IA/g (n = 24), and blood half-life was 33.1 ± 5.8 h (n = 24) (Table 1).

Ex vivo biodistribution was performed after the terminal PET/CT scan to corroborate the imaged-based quantitative data and to determine a more comprehensive tissue distribution of ^{86}Y-NM600 in nontumor tissues. Broad agreement was observed between quantitative PET/CT VOI analysis (Fig. 3) and ex vivo biodistribution (Fig. 4) in both magnitude and trend. However, the spleen, which was difficult to delineate using CT, showed similar uptake to that of the kidneys, approximately 5 %IA/g at 72 h after injection. Conversely, bone, which includes the contribution from the bone marrow, contained less than 2 %IA/g whereas the bone marrow VOI in the PET/CT analysis contained up to 5 %IA/g in some mouse strains, because of the characteristic partial-volume effects of ^{86}Y that are exacerbated by the small volume of the marrow.

Dosimetry Estimation

Because of a higher and more prolonged accumulation of ^{86}Y-NM600 in tumor tissues, Panc02 and EL4 had the largest ^{90}Y-NM600 estimates of dose per injected activity, 2.72 ± 0.33 Gy/MBq and 2.67 ± 0.32 Gy/MBq, respectively. The liver doses for all mouse strains investigated were greater than 3 Gy/MBq. However, the liver doses for NSG and FVB were significantly less, at 1.87 ± 0.11 and 2.04 ± 0.14 Gy/MBq, respectively. The kidney doses were on average between 1 and 2 Gy/MBq, and the bone marrow doses were less than 1 Gy/MBq (Fig. 5; Supplemental Table 1).

Toxicity Evaluation

A comprehensive set of studies was performed to interrogate potential acute systemic toxicities associated with the administration of ^{90}Y-NM600. Histology and complete blood count were analyzed from these cohorts at 5, 10, and 28 d after injection. Day 5 hematoxylin and eosin stains shows a reduction in cellularity in white pulp of the bone marrow and spleen, which recovered by days 10 and 28, respectively. However, the effects were mild and did not result in animal mortality. No evidence of morphologic change was observed in liver, kidneys, or intestine after treatment (Fig. 6A). Mice did not experience any significant weight change (data not shown). The toxicity results coupled with the dosimetry estimations indicate the feasibility of safely delivering 2–20 Gy to the tumors in these models with a single ^{90}Y-NM600 injection.

The complete blood count panels (Fig. 6B) at days 5, 10, and 28 were normalized by the control group, which was not treated. The white blood cell, lymphocyte, and platelet counts decreased out to day 10 below the control group but drastically increased at day 28. The red blood cells and hemoglobin did not appear to be affected by ^{90}Y-NM600. Overall, these results demonstrated that 9.25 MBq of

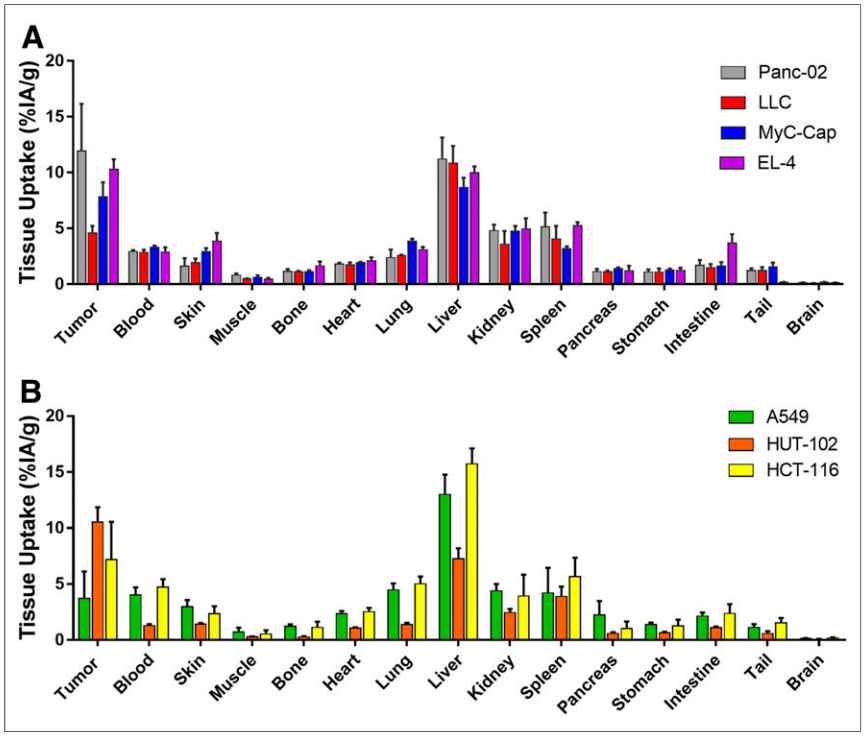

FIGURE 4. Ex vivo biodistribution was performed after final imaging time point at 66–68 h after injection. (A) Results of syngeneic models. (B) Results of human xenograft models. Trends in biodistribution are like that of in vivo analysis. Numeric data are presented as %IA/g (mean ± SD).

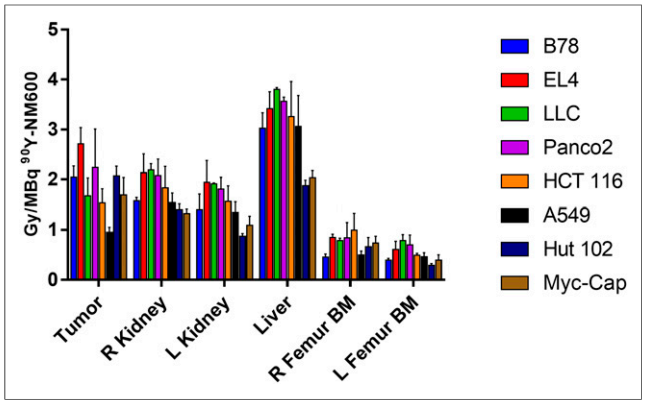

FIGURE 5. Dosimetry summary for tumor and organs at risk. Mean (± SD) absorbed dose per injected activity of ^{90}Y-NM600 is shown for each mouse tumor model.

^{90}Y-NM600 was well tolerated, owing to the minor and transient toxicities associated with administration of the TRT agent.

Efficacy Evaluation

In a 1-tumor model, in situ vaccine treatment consisting of XRT combined with an antitumor immunocytokine has been shown to result in complete cure, with immune memory in 90% of B78 melanoma–bearing mice (*14*). In the presence of a distant nonirradiated or metastatic tumor, there was surprisingly no response even at the primary vaccinated site in any of the mice. Subsequent studies revealed that regulatory T cells from peripheral tumors migrate to the primary tumor and block immune surveillance, thus preventing a response similar to that seen in the 1-tumor model (*15*). It has been shown that 2–3 Gy of radiotherapy can deplete tumor-specific regulatory T cells and renew the in situ vaccination effect (*15*).

In a follow-up efficacy study, we tested our ability to accurately and safely deliver an immunomodulatory dose of 2–3 Gy to B78 tumors by ^{90}Y-NM600 TRT. To corroborate the validity of our tumor dose calculations, we performed a benchmarking experiment in which one group of mice bearing B78 tumors received a 2.5-Gy single-fraction dose of XRT and another group was injected with activity of ^{90}Y-NM600 to deliver an equivalent cumulative dose. Tumor growth was monitored in both treatment arms and compared with the untreated controls. Although there was not a significant difference in tumor response between XRT- and TRT-treated mice, both treatments resulted in significant tumor growth delay compared with untreated controls (Fig. 7). These data confirmed our theranostic approach of using precision dosimetry to prescribe a delivered activity of ^{90}Y-NM600 that achieves biologic effects on the tumor comparable to that of an equivalent known dose of XRT.

DISCUSSION

Preclinical studies have shown that XRT can function as a method of in situ tumor vaccination that can enhance the efficacy of systemic immunotherapy (*14*). However, in the presence of multifocal disease, the collection of distant nonirradiated tumors may act as a reservoir of suppressive immune cell lineages that can antagonize this effect (*15*). This can be circumvented by irradiating all tumors (*15*), which is impractical to achieve using XRT without also inducing bone marrow depletion and systemic cytopenias. To enhance the cooperative interaction between in situ vaccination with XRT at a single tumor site and systemic immunotherapy, we aim to use TRT with radiolabeled alkylphosphocholines to deliver immunomodulatory radiation doses to all tumor sites regardless of anatomic location. In addition, immunomodulatory effects on the tumor microenvironment may occur at lower radiotherapy doses of between 2 and 5 Gy (*16,17*).

NM600, a new cancer-targeting theranostic alkylphosphocholine chelate, showed selective tumor accumulation with retention in all tumor models investigated. The maximum peak tumor uptake, approximately 9 %IA/g, is comparable to a radioiodinated alkylphosphocholine such as ^{124}I-NM404 (*18–20*). However, the peak tumor uptake can be reached as early as 24 h after injection, which is considerably sooner than radioiodinated alkylphosphocholines, which peak 72–96 h after injection. Both NM600 and NM404 are predominantly metabolized by the hepatobiliary system, as is indicated by elevated levels of PET signal within the liver and intestines and radioactivity within the feces. Although the liver signal of NM600 is higher than that of NM404 at 96 h after injection, the blood clearance of NM600 is much faster, leading to less blood retention and a potentially larger therapeutic window than for NM404, meaning that more radioactivity can be injected without causing toxicity. The blood concentration of NM404 is greater than 5 %IA/g at 244 h after injection (*20*) in similar xenograft models.

Dosimetry estimations showed that the largest absorbed dose per injected activity of ^{90}Y-NM600 was imparted to the liver regardless of the mouse strain. The relatively high dose estimations of Panc02 and EL4 warrant further investigation to test whether NM600 uptake is consistently elevated across all pancreatic cancer and lymphoma cell lines.

The toxicity evaluation of ^{90}Y-NM600 showed that the visible signs of acute toxicity in hematoxylin and eosin slides of nontumor tissues—toxicity that may be

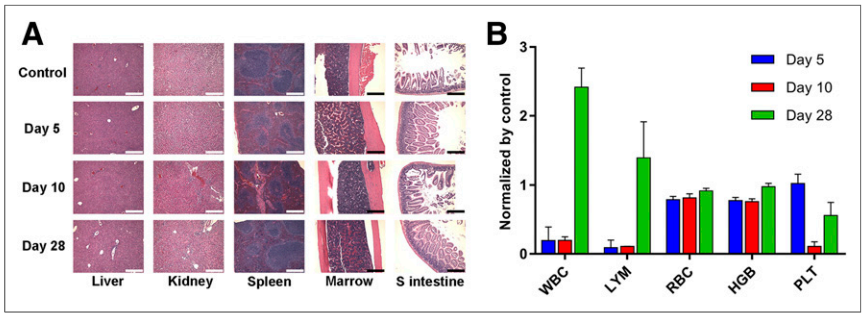

FIGURE 6. Toxicity assessment in naïve C57BL/6 mice administered ^{90}Y-NM600. (A) Hematoxylin and eosin staining of potential organs at risk was performed for mice given 9.25 MBq of ^{90}Y-NM600 IA at days 5, 10, and 28 after injection. Day 5 shows reduction in cellularity in white pulp of spleen and bone marrow, which were largely recovered at day 10. Images are displayed at ×20 magnification. (B) Complete blood count panel at days 5, 10, and 28 normalized by control group, which was not treated. White blood cells (WBC) and lymphocytes (LYM) decrease out to day 10 below control group but drastically increase at day 28—a finding that does not appear to be induced by radiation toxicity. However, platelets appear to be reduced at day 10 but recover by day 28. Red blood cells (RBC) and hemoglobin (HGB) do not appear to be affected by ^{90}Y-NM600.

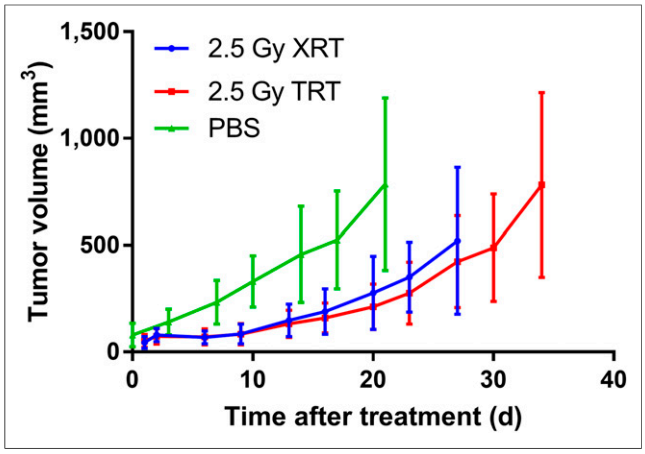

FIGURE 7. Tumor response of 2.5 Gy of ^{90}Y-NM600 or XRT compared with no treatment, phosphate-buffered saline (PBS). There is not much evidence of significant difference between XRT and TRT. However, volume slope of XRT was significantly lower than PBS slope (β = −15.63, SE = 3.97, P = 0.0001). Numeric data are presented as mm^3 (mean ± SD).

dose-limiting or of concern immunologically—were well tolerated. Since there were no evident toxicities within the organs of interest when a tumor cytotoxic injection of 9.25 MBq (250 μCi) of ^{90}Y-NM600 was administered, we can assume that the administered activities that are part of the TRT studies outlined in this work would not cause toxicity because they are well below 9.25 MBq. Therefore, we have evidence that subcytotoxic amounts of ^{90}Y-NM600 can deliver immunomodulatory tumor doses without causing systemic toxicity.

The tumor uptake mechanism of NM600, which appears to be ubiquitous to nearly all cancer types, could ultimately afford advantages over other agents that are targeted to specific pathways or receptors and whose efficacy is greatly impacted by inter- and intrapatient tumor heterogeneity. In addition, the chemical flexibility afforded by the DOTA chelate of NM600 facilitates the use of different radionuclides with different half-lives and radiobiologic properties, including α-emitters such as ^{225}Ac. Overall, our results suggest that NM600 is truly a unique agent that has the potential to positively impact many types of cancer either as a monotherapy or in combination with other therapies. In future studies, we will investigate the potential synergy of ^{90}Y-NM600 with a variety of immunotherapies in a variety of cancer types, including immunologically cold and hot tumors. The TRT preclinical treatment study in B78 demonstrated that the theranostic application of $^{86/90}$Y-NM600 accurately indicated 1.85 MBq for delivery of immunomodulatory doses of TRT (2–3 Gy), producing tumor responses equivalent to those delivered by XRT. This is particularly important when trying to rescue in situ tumor vaccination because the distant nonirradiated tumors that harbor tumor-specific regulatory T cells can be suppressed and the efficacy of systemic immunotherapy can be enhanced.

Because of the drastic difference in dose rates between XRT and TRT, it is not obvious that an equivalent absorbed dose of 2.5 Gy will result in biologically equivalent effects on tumor growth delay. Conventional radiobiology suggests that XRT should have a greater effect on tumor cell killing because of reduced potential for sublethal damage repair with higher dose-rate XRT (*21*). However, ultra-low-dose-rate brachytherapy has been shown effective as well, which can be attributed in part to cell-cycle synchronization (*22*). The dose rates that are delivered to B78 tumors by ^{90}Y-NM600 are even lower than ultra-low-dose-rate brachytherapy, suggesting that there may be another mechanism at play. We hypothesize that this mechanism may involve a more effective stimulation of antitumor immune response by the low-dose-rate TRT relative to XRT, and we are actively investigating this possibility now.

Our study has some limitations. First, partial-volume correction or positron range correction was not applied to the ^{86}Y-NM600 PET images; this can lead to quantitative inaccuracies in the VOI analysis and dosimetry estimations: a negative bias in tumor uptake values that will result in the underestimation of ^{90}Y-NM600 dosimetry in the organs of uptake. The long mean positron range of ^{86}Y (2.5 mm (*23*)) causes diminished spatial resolution, which leads to uncertainty in dosimetry estimates, especially in tumors or organs that are relatively small compared with the system resolution of the PET scanner (*24,25*). In addition, the long positron range of ^{86}Y can lead to spillover of radioactivity into adjacent tissues. For example, the kidneys, bone, or bone marrow may experience spillover from the tumor, depending on its location on the flank. Lastly, because the true activity distribution of ^{86}Y is effectively blurred because its positron range has not been corrected for, the resulting dose estimation for ^{90}Y is blurred too, which leads to increased cross-fire radiation between adjacent tissues. This can be seen in a subgroup of mice that had a flank tumor adjacent to the femur. The bone marrow VOI in the right femur had higher doses than the left femur in these cases. In larger species in which organs are generally farther from each other than in mice, the cross-fire effect caused by ^{90}Y will be lessened.

CONCLUSION

^{86}Y-NM600 coupled with a Monte Carlo dosimetry platform (RAPID) has the capability of precisely estimating the administered activity of ^{90}Y-NM600 that will deliver desired absorbed doses to the tumor microenvironment. The theranostic validation of NM600, coupled with its unique ability to selectively target a variety of cancer types, suggests that it may have the ability to safely and precisely immunomodulate the tumor microenvironment, presenting a unique opportunity for combination with immunotherapies.

DISCLOSURE

Support was provided by the University of Wisconsin Carbone Cancer Center (grant P30 CA014520), the University of Wisconsin (20/20 grant), and the Beau Biden Cancer Moonshot Initiative (U01CA233102). Jamey Weichert is the cofounder of Archeus Technologies, which owns the rights to the alkylphosphocholine chelates discussed herein. Joseph Grudzinski and Reinier Hernandez are consultants for Archeus Technologies. Zachary Morris is a scientific advisor to Archeus Technologies. No other potential conflict of interest relevant to this article was reported.

ACKNOWLEDGMENTS

We thank the UW Small Animal Imaging Facility for its assistance.

KEY POINTS

QUESTION: Does ^{90}Y-NM600 have the potential to safely and selectively deliver the required tumor dose to immunomodulate the tumor microenvironment?

PERTINENT FINDINGS: ^{86}Y-NM600 coupled with a Monte Carlo dosimetry platform (RAPID) can precisely estimate the administered activity of ^{90}Y-NM600 that will deliver desired absorbed doses to the tumor microenvironment. The theranostic validation of NM600, coupled with its unique ability to selectively target a variety of cancer types, suggests that it may have the ability to safely and precisely immunomodulate the tumor microenvironment, presenting a unique opportunity for combination with immunotherapies.

IMPLICATIONS FOR PATIENT CARE: ^{90}Y-NM600 may improve outcomes of patients who are undergoing immunotherapy by immunomodulating the tumor microenvironment through delivering targeted radiation to many tumor types regardless of tumor location.

REFERENCES

1. Kirschner AS, Ice RD, Beierwaltes WH. Radiation dosimetry of ^{131}I-19-iodocholesterol. *J Nucl Med.* 1973;14:713–717.
2. Carrasco MP, Jiménez-López JM, Ríos-Marco P, Segovia JL, Marco C. Disruption of cellular cholesterol transport and homeostasis as a novel mechanism of action of membrane-targeted alkylphospholipid analogues. *Br J Pharmacol.* 2010;160:355–366.
3. Gajate C. The antitumor ether lipid ET-18-OCH3 induces apoptosis through translocation and capping of Fas/CD95 into membrane rafts in human leukemic cells. *Blood.* 2001;98:3860–3863.
4. Reis-Sobreiro M, Roué G, Moros A, et al. Lipid raft-mediated Akt signaling as a therapeutic target in mantle cell lymphoma. *Blood Cancer J.* 2013;3:e118.
5. van der Luit AH, Budde M, Ruurs P, Verheij M, van Blitterswijk WJ. Alkyllysophospholipid accumulates in lipid rafts and induces apoptosis via raft-dependent endocytosis and inhibition of phosphatidylcholine synthesis. *J Biol Chem.* 2002; 277:39541–39547.
6. Aluicio-Sarduy E, Hernandez R, Valdovinos HF, et al. Simplified and automatable radiochemical separation strategy for the production of radiopharmaceutical quality ^{86}Y using single column extraction chromatography. *Appl Radiat Isot.* 2018;142:28–31.
7. Haraguchi M, Yamashiro S, Yamamoto A, et al. Isolation of GD3 synthase gene by expression cloning of GM3 alpha-2,8-sialyltransferase cDNA using anti-GD2 monoclonal antibody. *Proc Natl Acad Sci USA.* 1994;91:10455–10459.
8. Partecke LI, Sendler M, Kaeding A, et al. A syngeneic orthotopic murine model of pancreatic adenocarcinoma in the C57/BL6 mouse using the Panc02 and 6606PDA cell lines. *Eur Surg Res.* 2011;47:98–107.
9. Watson PA, Ellwood-Yen K, King JC, Wongvipat J, LeBeau MM, Sawyers CL. Context-dependent hormone-refractory progression revealed through characterization of a novel murine prostate cancer cell line. *Cancer Res.* 2005;65:11565–11571.
10. Rizk S, Maalouf K, Baydoun E. The antiproliferative effect of kefir cell-free fraction on HuT-102 malignant T lymphocytes. *Clin Lymphoma Myeloma.* 2009;9(suppl 3):S198–S203.
11. Bednarz B, Grudzinski J, Titz B, Besemer A. Monte Carlo-based radiation dosimetry for preclinical trials of radiohalogenated pharmaceuticals. *Trans Am Nucl Soc.* 2013;108:43–44.
12. Bednarz B, Grudzinski J, Marsh I, et al. Murine-specific internal dosimetry for preclinical investigations of imaging and therapeutic agents. *Health Phys.* 2018;114:450–459.
13. Besemer AE, Yang YM, Grudzinski JJ, Hall LT, Bednarz BP. Development and validation of RAPID: a patient-specific Monte Carlo three-dimensional internal dosimetry platform. *Cancer Biother Radiopharm.* 2018;33:155–165.
14. Morris ZS, Guy EI, Francis DM, et al. In situ tumor vaccination by combining local radiation and tumor-specific antibody or immunocytokine treatments. *Cancer Res.* 2016;76:3929–3941.
15. Morris ZS, Guy EI, Werner LR, et al. Tumor-specific inhibition of in situ vaccination by distant untreated tumor sites. *Cancer Immunol Res.* 2018;6: 825–834.
16. Liu S-Z. Nonlinear dose-response relationship in the immune system following exposure to ionizing radiation: mechanisms and implications. *Nonlinearity Biol Toxicol Med.* 2003;1:71–92.
17. Rodriguez-Ruiz ME, Garasa S, Rodriguez I, et al. Intercellular adhesion molecule-1 and vascular cell adhesion molecule are induced by ionizing radiation on lymphatic endothelium. *Int J Radiat Oncol Biol Phys.* 2017;97:389–400.
18. Weichert JP, Clark PA, Kandela IK, et al. Alkylphosphocholine analogs for broad-spectrum cancer imaging and therapy. *Sci Transl Med.* 2014;6: 240ra75.
19. Grudzinski J, Marsh I, Titz B, et al. CLR 125 Auger electrons for the targeted radiotherapy of triple-negative breast cancer. *Cancer Biother Radiopharm.* 2018; 33:87–95.
20. Grudzinski JJ, Floberg JM, Mudd SR, et al. Application of a whole-body pharmacokinetic model for targeted radionuclide therapy to NM404 and FLT. *Phys Med Biol.* 2012;57:1641–1657.
21. Pouget J-P, Lozza C, Deshayes E, Boudousq V, Navarro-Teulon I. Introduction to radiobiology of targeted radionuclide therapy. *Front Med (Lausanne).* 2015;2:12.
22. Chapman JD. Single-hit mechanism of tumour cell killing by radiation. *Int J Radiat Biol.* 2003;79:71–81.
23. Jødal L, Le Loirec C, Champion C. Positron range in PET imaging: non-conventional isotopes. *Phys Med Biol.* 2014;59:7419–7434.
24. Lubberink M, Herzog H. Quantitative imaging of ^{124}I and ^{86}Y with PET. *Eur J Nucl Med Mol Imaging.* 2011;38(suppl):S10–S18.
25. Frey EC, Humm JL, Ljungberg M. Accuracy and precision of radioactivity quantification in nuclear medicine images. *Semin Nucl Med.* 2012;42:208–218.